optics

MDPI

Article

Dynamic Excitation of Surface Plasmon Polaritons with Vector Laguerre–Gaussian Beams

Aldo Peña-Ramírez [1], Tingting Zhai [2,†], Rafael Salas-Montiel [2,*] and Víctor Ruiz-Cortés [1]

[1] Department of Optics, Division of Applied Physics, Centro de Investigación Científica y de Educación Superior de Ensenada—CICESE, Ensenada 22860, Mexico
[2] Laboratory Light, Nanomaterials, and Nanotechnology—L2n CNRS UMR 7076, Université de Technologie de Troyes, 10004 Troyes, France
* Correspondence: rafael.salas@utt.fr
† Current address: Department of Information Technology (INTEC), Ghent University—IMEC, 9052 Ghent, Belgium.

Abstract: We investigate the dynamic excitation of surface plasmon polaritons (SPPs) using vector Laguerre–Gauss (LG) beams, which offer unique properties for manipulating the polarization and spatial distribution of light. Our study demonstrates the efficient coupling of SPPs with LG beams, characterized by their azimuthal and radial indices (m, p), as well as polarization distribution type. Numerical simulations reveal that the vector nature of LG beams enables selective excitation of SPPs, depending on the polarization type of the beam. Experimental verification of our simulations is achieved using a gold circular Bragg grating and a spatial light modulator that generates vector LG beams. Leakage radiation imaging demonstrates the potential of vector LG beams for dynamic SPP excitation and manipulation. This study opens novel ways for the control of SPPs in plasmonic devices, such as modulators, and nanophotonic circuits.

Keywords: plasmonics; optics modes; structured light; beam shaping; physical optics

Citation: Peña-Ramírez, A.; Zhai, T.; Salas-Montiel, R.; Ruiz-Cortés, V. Dynamic Excitation of Surface Plasmon Polaritons with Vector Laguerre–Gaussian Beams. *Optics* **2024**, *5*, 523–533. https://doi.org/10.3390/opt5040039

Academic Editor: Costantino De Angelis

Received: 27 August 2024
Revised: 21 October 2024
Accepted: 7 November 2024
Published: 21 November 2024

1. Introduction

Surface plasmon polaritons (SPPs), surface waves that result from the interaction between light photons and the collective oscillation of free electrons at the metal/dielectric interface [1], have been the subject of intensive research in the recent twenty years basically because they hold the promise of being the next chip-scale technology [2] down to the nanometer [3] and the subwavelength scale [4]. From the device point of view, the metal/dielectric interface serves as a channel (i.e., a plasmonic waveguide) that carries information (i.e., the surface wave). To excite SPPs into plasmonic devices, light illuminating the interface from the dielectric medium must equal the frequency of the SPPs, and the component of the wavevector of the incident light parallel to the surface (i.e., k_x) must equal the wavevector of the SPPs (k_{SPP}) [5]. To equal or match these wavevectors, special arrangements need to be used to obtain equality as the SPP wavevector is larger than that of the component of the wavevector of incident light. These arrangements provide the extra wavevector needed for wavevector matching. In addition to the bulky Kretschmann [6] and Otto configurations [7], many surface arrangements have been proposed to excite SPPs, such as diffraction gratings [1,8,9], diffraction of surface features [9,10], holes in metals [11], dielectric waveguides [12–14], and near-field scanning optical microscope probes [15–17]. However, most illumination schemes are carried out with spatially homogeneous polarized light such as linearly, circularly, and elliptically polarized beams. The excitation and manipulation of SPPs can be extended with incident light spatial amplitude and phase distributions [18–20], as well as with spatial inhomogeneous polarization distribution such as that presented in optical vector beams (VBs) [21–24]. The radially vector beam is one of the most investigated vector beams and has been used to excite and focus SPPs in a bull's

eye plasmonic antenna [25] and dark modes in nanorod trimers [26]. Vectorial beams can be generated via two methods: passive generators that convert the fundamental Gaussian beams into VBs by using dynamic or geometric phase plates, metasurfaces, and active laser generators [18]. In addition, interferometric approaches typically combine a superposition of orthogonal linearly polarized beams to generate VBs [27]. These methods, however, are designed to generate specific VBs. The use of spatial light modulators (SLMs) is an efficient way to generate VBs by converting fundamental Gaussian beams [28]. The observation of optical spin symmetry breaking in plasmonic nanoapertures was demonstrated with VBs whose phase was modulated by an SLM [20,29]. Active control over the amplitude and phase of SPPs was also demonstrated with the use of digital SLMs [30–33]. Most of these schemes, however, used the scalar distribution of the complex beams, namely amplitude and phase.

In this work, we used spatially varying polarization distribution vector Laguerre–Gaussian (LG) beams to dynamically excite surface plasmon polaritons in a circular plasmonic Bragg grating. The vector LG beams, with a spatially inhomogeneous polarization distribution, were generated through the dynamic conversion of a fundamental Gaussian beam with an SLM. Novel intensity and polarization patterns were produced through the SLM, and the excitation of SPPs was experimentally investigated using leakage radiation microscopy (LRM). In addition, we numerically performed a systematic study of the excitation of SPPs with vector LG beams.

2. Materials and Methods

2.1. Design, Fabrication, and Characterization of the Circular Bragg Grating

The configuration we choose to demonstrate the dynamic control for the excitation of SPPs is a circular Bragg grating configuration (Figure 1a). When a local radially polarized part of the vector beam illuminates the circular Bragg grating, the local field is transverse magnetic (TM) polarized with respect to the edge of the circular grating. This local polarization can thus excite SPPs efficiently. The SPPs propagate through the center of the circular grating and generate a highly focused SPP through constructive interferences [25]. The focusing spot field is enhanced relative to that when a linear polarized beam is used as an excitation beam. The period of the grating is calculated to fulfill the phase-matching condition $\beta_{SPP} = k_0 \sin\theta \pm \frac{2\pi}{a}$ or the excitation of SPPs, where $\beta_{SPP} = k_0 n_{SPP}$ is the SPP wavevector, and k_0 is the wavevector of the incident field. Excitation efficiencies as high as 0.5 are obtained with such gratings [9]. At a wavelength of λ = 780 nm, the calculated effective index of the SPP in the air–metal interface in a 50 nm thick gold (Au) thin film is n_{SPP} = 1.021857 + i0.00135679, and thus the period $a = \lambda / n_{SPP}$ = 0.764 μm was obtained (see the Supplementary Materials). The grating thus has a period of a = 0.764 μm with a duty cycle of 0.5, a thickness of 20 nm, and consists of a number N = 14 concentric rings (Figure 1). The inner ring has a radius of 20 μm. The circular grating is made of Au and is patterned on top of a 50 nm thick Au thin film on a cover slide glass substrate. A vector LG beam is incident from the top of the circular grating at an incident wavelength of 780 nm and an angle of incidence θ = 0 (Figure 1a). For the sample fabrication, we started with Au deposition of a thin film of 50 nm via Joule effect evaporation on top of a cover slide. We then used electron beam lithography (EBL by Raith eLINE) to define the concentric rings. We used PMMA resist with a thickness of about 180 nm and the following EBL parameters: electron gun tension 20 kV, aperture 10 μm, and step size 0.0064 μm. After the exposition, the pattern was developed on an MIBK:IPA (1:3) developer for 60 s. Finally, a second Au deposition and lift-off process was carried out to define the Au circular Bragg grating with a thickness of 20 nm (Figure 1b,c).

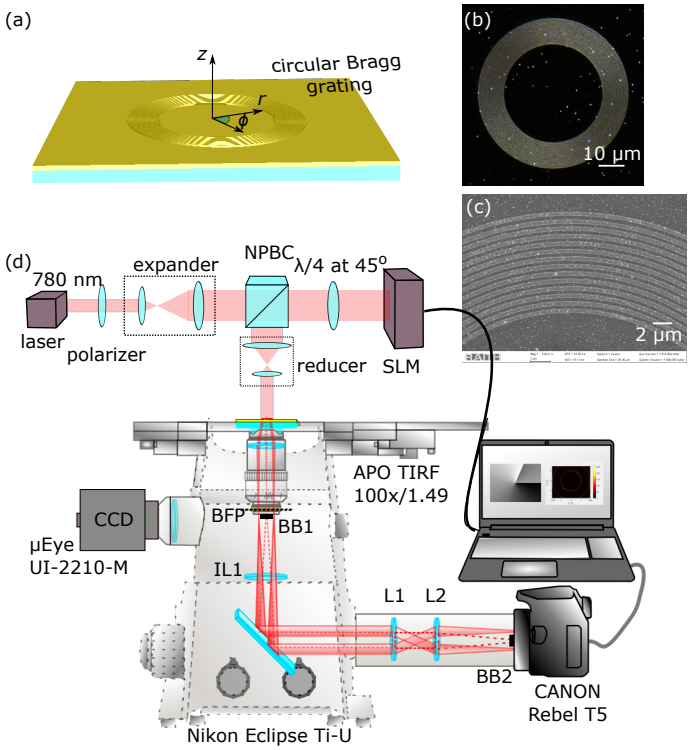

Figure 1. Dynamic excitation of surface plasmon polaritons with vector Laguerre–Gaussian beams. (**a**) Schematic of the circular plasmonic Bragg grating on gold thin film. The thickness of the grating and thin film are 20 nm and 50 nm, respectively. The grating consists of 14 concentric rings with a period of a = 0.764 μm and 0.5 duty cycle. The structure is dynamically excited with vector LG beams at normal incidence. (**b**) Optical and (**c**) scanning electron microscope images of the grating. Zoom on the grating area. (**d**) Scheme of the setup for the dynamic excitation of SPPs with vector LG beams. A spatial light modulator (SLM) is used to form the vector LG beams. Red optical path shows the path for the Fourier plane.

2.2. Leakage Radiation Microscopy

The setup for the measurement of the dynamic excitation of SPPs is based on the use of an SLM to generate vector LG beams (Figure 1d). Specifically, we used the Hamamatsu, Japan, LCOS-SLMX10468 with 792 × 600 pixels and 256 gray levels (8 bits). An input beam is reshaped with the SLM into the desired vector LG beam [34]. The SPPs' intensity distribution near the air/gold interface was directly measured via the leakage radiation microscopy (LRM) technique. In this technique, the propagating SPPs at the air/gold interface leak through the Au thin film into the glass substrate due to boundary conditions and conservation of the in-plane wavevector along two interfaces [35–37]. The leakage radiation from the SPPs is detected in the far field in both the direct space with the μEye CCD camera, UI-2210-M and in the Fourier space with the Canon Rebel T5 camera, which uses two lens to make the object focal plane coincide with the back focal plane (BFP). The leaked radiation is collected by a large aperture oil immersion microscope objective (MO2, APO TIRF 100 × NA = 1.49) and an image is taken with a μEye CCD camera. A removable beam blocker (BB1) was placed close to the BFP of the microscope objective (MO2) to filter the directly transmitted light passing through the sample and thus to image only the distribution of the LR. If the beam blocker BB1 is removed, a reference light beam propagates to the LR image plane and illuminates the CCD camera, which generates a fringe pattern due to the interference of the reference beam and the LR of the SPPs, as described by Garcia-Ortiz et al. [38]. To obtain images of the Fourier plane, an afocal system (L1 and L2 lenses) was placed on one of exit ports of the inverted microscope that, together with the IL1 lens, allow us the imaging of the back focal plane (BFP) of the MO2 onto the CCD of a Canon Rebel T5 camera. In this way, it is possible to visualize

the Fourier plane corresponding to the excited SPPs in the sample. In addition, a beam blocker (BB2) was placed close to the Fourier plane to eliminate the contribution of the light transmitted directly through the sample. The angle at which the radiation leaks is given by $\sin[\theta_{LR}(\lambda)] = \mathrm{Re}[n_{SPP}(\lambda)]/n_{glass}$, which is $\theta_{LR}(\lambda) = 43.8°$ in our case.

2.3. Vector $LG_{(p,m)}$ Beams

To gain physical insight of our experimental results, we perform numerical simulations of the excitation of SPPs with vector LG beams with the use of a 3D finite-difference time-domain (FDTD) method. The vector LG beams are paraxial solutions of the vector Helmholtz's equation in cylindrical coordinates [39]. Specifically, these VBs have a spatially varying polarization distribution with cylindrical symmetry given by [40]:

$$\mathbf{E}_{(p,m)}(r,\phi,z) = U_{(p,m)}(r,z)\mathbf{P}_m(\phi), \tag{1}$$

where $U_{(p,m)}(r,z)$ is the radial and axial distribution, and $\mathbf{P}_m(\phi)$ is the inhomogeneous polarization distribution in the cross-section of the vector beam. $U_{(p,m)}(r,z)$ is given by

$$U_{(p,m)}(r,z) = \sqrt{\frac{2p!}{\pi(p+m)!}}\frac{1}{w(z)}\exp\left[\frac{-r^2}{w^2(z)}\right]\left[\frac{\sqrt{2}r}{w(z)}\right]^{|m|}L_p^{|m|}\left[\frac{2r^2}{w^2(z)}\right], \tag{2}$$

where r is the radial direction, ϕ is the azimuthal angle, z is the distance from the waist, p and m are the radial and azimuthal mode numbers, respectively, and the distribution $\mathbf{P}_m(\phi)$ is defined as

$$\mathbf{P}_m(\phi) = \begin{cases} +\cos(m-1)\phi\hat{e}_\phi - \sin(m-1)\phi\hat{e}_r, & \text{for type I} \\ +\cos(m+1)\phi\hat{e}_\phi + \sin(m+1)\phi\hat{e}_r, & \text{for type II} \\ +\sin(m-1)\phi\hat{e}_\phi + \cos(m-1)\phi\hat{e}_r, & \text{for type III} \\ -\sin(m+1)\phi\hat{e}_\phi + \cos(m+1)\phi\hat{e}_r, & \text{for type IV} \end{cases} \tag{3}$$

where $\hat{e}_\phi$ and $\hat{e}_r$ are the unit vectors along the azimuthal and radial directions, respectively. The local state of polarization is linear, but there is an azimuthal variation in the polarization direction. Here, we consider radial $p = 0$ and azimuthal indices $m = [1, 2, 3, 4]$. Also, we consider a wavelength of 780 nm and a beam waist of 30 µm (Figure 2).

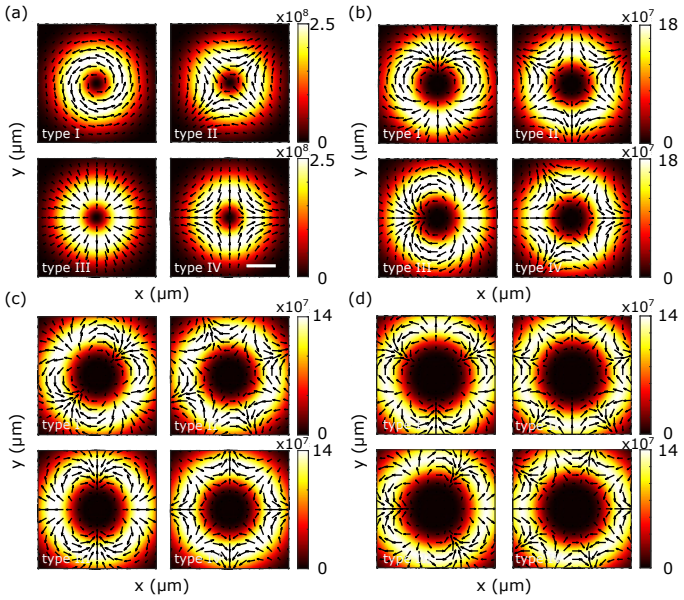

Figure 2. Calculated intensity and polarization distributions of vector LG beams $p = 0$ and (**a**) $m = 1$, types I–IV, (**b**) $m = 2$, types I–IV, (**c**) $m = 3$, types I–IV, and (**d**) $m = 4$, types I–IV. Scale bar is 25 µm.

For m = 1, types I and III correspond to azimuthally and radially polarized beams, respectively. They have an identical amplitude distribution, and the direction of local polarization at each point in the beam cross-section is orthogonal between the two beams [41]. For m = 1, types II and IV correspond to hybrid vector beams [40] with an identical amplitude distribution, and the direction of local polarization is also orthogonal between these two beams. Only the local polarization perpendicular to the grating edge can excite SPPs. We followed the code in reference [42] and we implemented the vector LG beams using Equations (1)–(3) in 3D FDTD solutions via Lumerical with proper cylindrical to Cartesian coordinate transformations. We fixed the calculation window of size 90 μm in the x and y axes, and 2 μm in the vertical z axis. Gold was modeled with the permittivity constant from ref. [43]. The plane of the source vector LG beam was placed 0.2 μm above the surface of the grating, and a field monitor was placed in the glass substrate, at 30 nm below the Au/glass interface to simulate the LRM imaging. The data from the field monitor in the glass substrate were decomposed into a series of plane waves that propagated at different angles. The plane wave outside the numerical aperture NA = 1.49 was discarded from the image plane to simulate our experimental setup. In addition, we also kept the data from the near-field distribution of the SPPs, both amplitude and phase distributions. We placed three field monitors of sizes 90 μm × 90 μm, 40 μm × 40 μm, and 10 μm × 10 μm to observe the extend of the SPP fields. Although we used a high NA, the near and far fields are quite different. To obtain the image in the Fourier space, we used far-field projection, which projects the field in the far field and takes the spatial Fourier transform. We used the Fourier-transformed field to plot the image in k-space.

3. Results and Discussion

3.1. Numerical Simulations and Vector $LG_{(p=0,m=1,2,3,4)}$ Beams

We start this section with the results of the numerical simulations of the excitation of SPPs with vector $LG_{(p,m)}$ beams. We simulated vector beams with radial p = 0 and azimuthal indices m = 1, 2, 3, and 4. We used the polarization distributions as described in Equation (3). Each type has an angular dependence of polarization distribution $\theta_p(\phi)$, which is a local angle of the polarization vector. For types I, II, III, and IV, the angular dependencies are $\theta_p = m\phi + \pi/2$, $\theta_p = -m\phi + \pi/2$, $\theta_p = m\phi$, and $\theta_p = -m\phi$, respectively. In Figure 3, we plotted the distribution of the electric field in the center of the grating for vector $LG_{(0,[1,2,3,4])}$ type I to IV beams.

For m = 1, types I and III with $\theta_p = m\phi + \pi/2$ and $\theta_p = m\phi$ correspond to the well-known azimuthally and radially polarized beams. Hybrid vector beams are obtained for types II and IV with $\theta_p = -m\phi + \pi/2$ and $\theta_p = -m\phi$, respectively. Because the polarization distribution of the vector $LG_{(0,1)}$ beams of type I does not present a local TM polarization (i.e., polarization vector perpendicular to the grating), SPPs are not excited (Figure 3a). In contrast, for type III beams, all local polarization vectors are perpendicular to the grating and, thus, SPPs are excited from all angles (Figure 3c).

For vector $LG_{(0,1)}$ type II beams, maximum excitation of SPPs comes from angles $\pi/4$, $3\pi/4$, $5\pi/4$, and $7\pi/4$ rad (Figure 3b) as the angle of the local polarizations are $\theta_p = \pi/4$, $\theta_p = -\pi/4$, $\theta_p = -3\pi/4$, and $\theta_p = -5\pi/4$ rad, respectively, at these angles. Finally, for type IV beams, maximum excitation of SPPs comes from angles 0, $\pi/2$, π, and $3\pi/2$ rad (Figure 3d) as the angle of local TM polarizations are θ_p = 0, $-\pi/2$, $-\pi$, and $-3\pi/2$ rad, respectively, at these angles. It is interesting to note that the electric and magnetic field lines at the center of the grating follow the local polarization distribution of the incident field. In the Supplementary Materials, the electric field lines in the center of the grating can be seen in Figures S3–S6 for types I, II, III, and IV, where the maps represent the absolute values of the magnetic field.

For m = 3, type I (type III), SPPs are excited from four angles, $\pi/4(0)$, $3\pi/4(\pi/2)$, $5\pi/4(\pi)$, and $7\pi/4(3\pi/2)$ rad (Figure 3i,k), as the angle of the local polarizations are $\theta_p = 5\pi/4(0)$, $11\pi/4(3\pi/2)$, $17\pi/4(3\pi)$, and $23\pi/4(9\pi/2)$ rad, respectively, at these angles. For m = 3, type II (and IV), SPPs are excited from eight angles, $\pi/8(0)$, $3\pi/8(\pi/4)$,

$5\pi/8(\pi/2)$, $7\pi/8(3\pi/4)$, $9\pi/8(\pi)$, $11\pi/8(5\pi/4)$, $13\pi/8(3\pi/2)$, and $15\pi/8(7\pi/4)$ rad (Figure 3j,l), as the angle of the local polarizations are $\theta_p = \pi/8(0)$, $-5\pi/8(-3\pi/4)$, $-11\pi/8(-3\pi/4)$, $-17\pi/8(-9\pi/4)$, $-23\pi/8(-3\pi)$, $-29\pi/8(-15\pi/4)$, $-35\pi/8(-9\pi/2)$, and $-41\pi/8(-21\pi/4)$ rad, respectively, at these angles. Again, the electric and magnetic field lines at the center of the grating follow the local polarization distribution of the incident field.

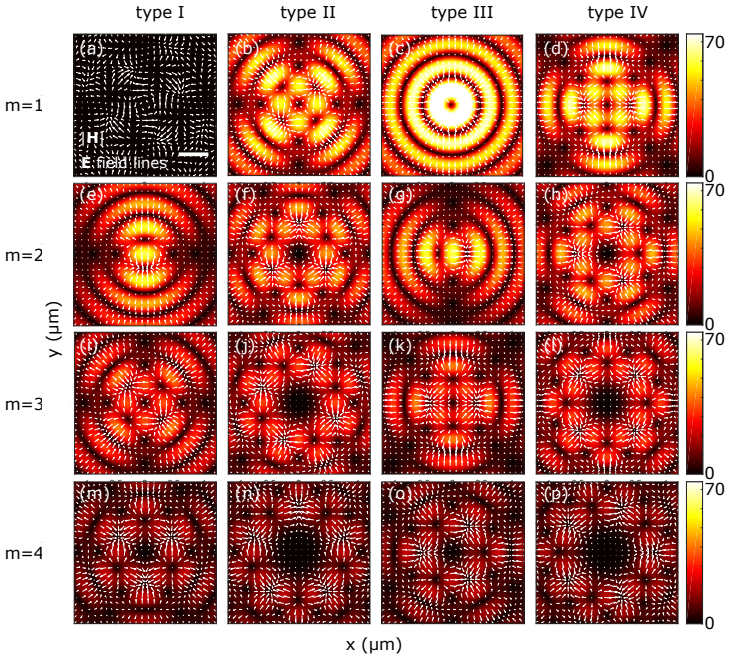

Figure 3. Excitation of surface plasmon polaritons with type I–IV vector $LG_{(0,[1,2,3,4])}$ beams. Distribution of the electric field and magnetic field lines for vector $LG_{(0,m)}$ beams (**a**) $m = 1$, type I, (**b**) $m = 1$, type II, (**c**) $m = 1$, type III, and (**d**) $m = 1$, type IV, (**e**) $m = 2$, type I, (**f**) $m = 2$, type II, (**g**) $m = 2$, type III, and (**h**) $m = 2$, type IV, (**i**) $m = 3$, type I, (**j**) $m = 3$, type II, (**k**) $m = 3$, type III, and (**l**) $m = 3$, type IV, (**m**) $m = 4$, type I, (**n**) $m = 4$, type II, (**o**) $m = 4$, type III, and (**p**) $m = 4$, type IV. Scale bar is 500 nm.

As seen in Figure 3, the electric field maps are different for each incident vector LG beam. The direction of excitation of SPPs follows the vector distributions. For instance, for incident vector LG beams with $m = 1$, types II and IV, the polarization distributions present four local vector directions perpendicular to the circular grating and, therefore, four peaks can be seen in the electric field maps at $\theta = n\pi/4$ with $n = 1$, 3, 5, and 7 for type II and $\theta = n\pi/2$ with $n = 0$, 1, 2, and 3 for type IV. The magnetic field lines circulate around each peak (see the Supplementary Materials). In addition to the electric field maps, we plotted the magnetic field maps in the Supplementary Materials. In these maps, we overlapped the electric field lines. Also, in the Supplementary Materials, we plotted the real part and phase of the z-component of the electric and magnetic field of the excited SPPs in the circular Bragg grating for each of the incident vector $LG_{(0,m=1,2,3,4)}$ beams for types I to IV. In the real part and phase of the principal component, we see not only the direction of excitation of SPPs but also the orientation of the direction of the polarization vector.

3.2. Experimental Results with LRM, Incident Vector $LG_{(p=0,m=1)}$ Beams

An optical microscope image of the Bragg grating in shown in Figure 4a. The two circumferences represent the inner and outer rings. The inner ring radius is 20 μm. We particularly focus on the experimental results, and we show the excitation of SPPs with vector beams $LG_{(0,1)}$ type III (Figure 4b) and I (Figure 4c). We observe the excitation of SPPs thanks to the extra momentum added by the Bragg grating. We also observe the propagation of the excited SPPs towards the center of the grating for type III beams, whereas no excitation of SPPs is obtained for type I beams, as expected.

Because the CDD camera not only detects the leakage radiation beam but also the incident beam, an interference pattern is formed due to the interference between the incident beam and the backward radiated field or leakage radiation. The collection of the incident field decreases the contrast of the LR images.

As described in Section 2.2, we measured the excitation of SPPs with LRM both in the direct (see magnified image in Figure 5b,e) and Fourier (Figure 5c,f) spaces.

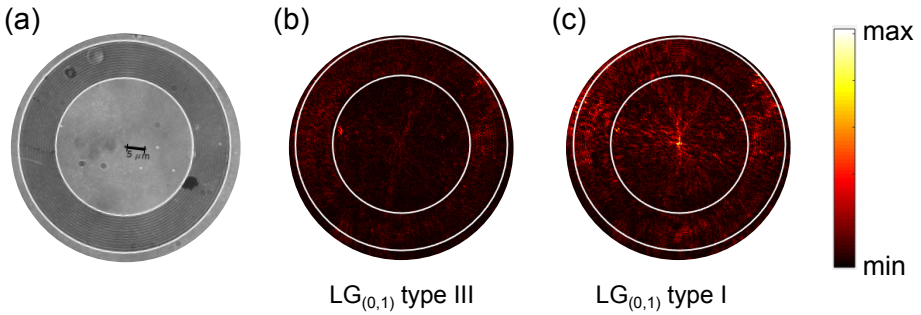

Figure 4. Experimental excitation of surface plasmon polaritons. (**a**) Optical image of the gold Bragg grating with a period of 764 nm. The two circumferences represent the inner and outer ring of the grating. Leakage radiation imaging of the excitation of SPPs with vector $LG_{(0,1)}$ (**b**) type III and (**c**) type I beams. Only type III beams excite SPPs.

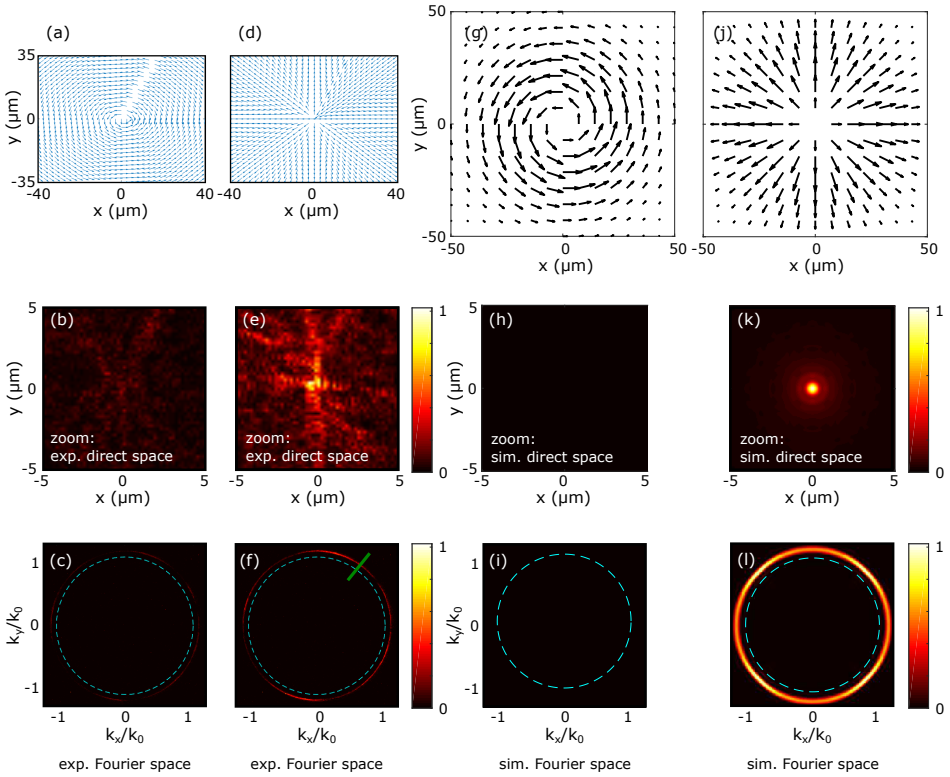

Figure 5. Experimental excitation of surface plasmon polaritons. Type I and III vector $LG_{(0,1)}$ beams. Experimental distribution of polarization of the incident field types (**a**) I and (**d**) III. Leakage radiation microscopy images of the excitation of SPPs in (**b**) the direct and (**c**) Fourier spaces for the type I and (**e**,**f**) for type III beams. Scheme of the incident fields for simulations of type (**g**) I and (**j**) III beams. Corresponding results of the excitation of SPPs in the (**h**,**k**) direct and (**i**,**l**) Fourier spaces.

In the Fourier space image, the map in a circumference shape confirms the excitation of SPPs in all k_x and k_y directions (Figure 5f). A profile along the green line provides a measure of the propagation length of SPPs [35]. We thus extracted a cross-cut and fitted with a Lorentz curve, where the reciprocal of the full width at half maximum (FWHM)

of the Lorentzian gives the propagation length (see the Supplementary Materials). We obtained a propagation length of 13.04 µm. This value coincides with the calculated one (see the Supplementary Materials, Figure S1). In Figure 5g–l, we show the results from the 3D FDTD simulations. The scheme of the distribution of polarization used in the simulation is plotted in Figure 5g for $LG_{(0,1)}$ type I beams and in Figure 5j for $LG_{(0,1)}$ type III beams. The simulated direct (Figure 5k) and Fourier space images (Figure 5l) coincide with the measured results.

To further demonstrate the directional control of the excitation of SPPs, we programmed the SLM to interpose sections (like slices in a circle chart) of vector $LG_{(0,1)}$ type I and III beams. The section with a local distribution of type III beams is expected to excite SPPs (Table 1). In Figure 6, we show the experimental results for four different divisions of polarization distributions, which are named D1 for a distribution for a six-twelfth $LG_{(0,1)}$ type I beam and a six-twelfth $LG_{(0,1)}$ type III beam (Figure 6a); D2 for a four-eighth $LG_{(0,1)}$ type I beam and a four-eighth $LG_{(0,1)}$ type III beam (Figure 6b); D3 with a two-quarter $LG_{(0,1)}$ type I beam and a two-quarter $LG_{(0,1)}$ type III beam (Figure 6c); and D4 with a one-half plane $LG_{(0,1)}$ type I beam and a one-half $LG_{(0,1)}$ type III beam (Figure 6d).

Table 1. Graphical representation of the experimental incident polarization distributions.

D1	D2	D3	D4
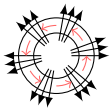	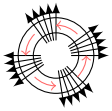	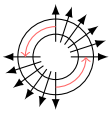	

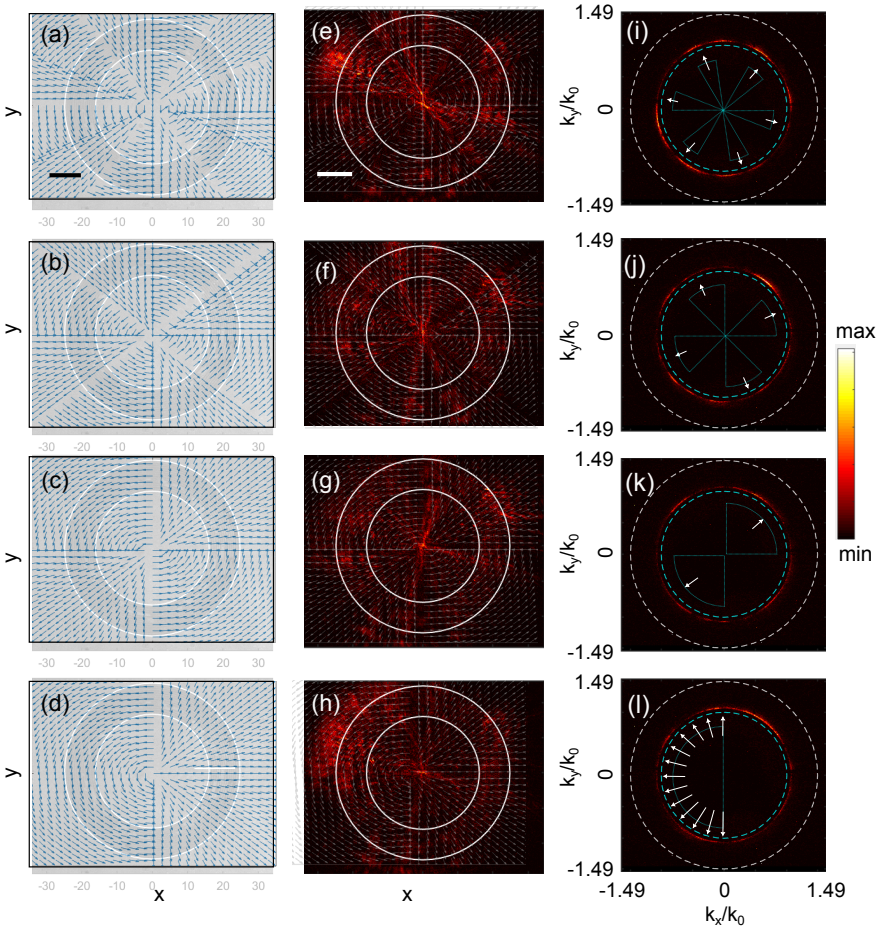

Figure 6. Excitation of SPPs with combinations of vector $LG_{(0,1)}$ type I and III beams. Scheme of distributions (**a**) D1, (**b**) D2, (**c**) D3, and (**d**) D4. The white lines represent the inner and outer grating

rings. Leakage radiation images of SPPs in (**e**–**h**) the direct and (**i**–**l**) Fourier spaces for distributions D1, D2, D3, and D4, respectively. Arrows indicate the sections where leakage radiation was detected. Insets in (**e**–**h**) are magnifications in the center of the grating. Scale bar is 10 μm in (**a**–**h**).

As expected, only the local polarization distribution where the polarization vector is perpendicular to the grating excites SPPs, while the other parts with a vector $LG_{(0,1)}$ type I beam polarization distribution do not excite SPPs. The selective excitation of SPPs is more clearly identified in the Fourier space images. In Figure 6i–l, the six, four, two, and one sections of distributions D1, D2, D3, and D4 are indicated with arrows. We performed 3D FDTD with distributions D1 to D4 (see the Supplementary Materials). The discrepancy between experiments and simulations is caused mainly by the misalignment between the optical axis of the incident beam and the axis of the center of the grating. We support this statement based on the numerical simulations conducted with an incident beam with a misalignment of $\Delta x = -10$ μm and $\Delta x = +10$ μm, only along the x-axis (see the Supplementary Materials). A misalignment towards negative values along the x-axis will produce more regions of incident type III beam overlapping with the grating and, thus, excite SPPs (Figure S30g–i in the Supplementary Materials). In contrast, a misalignment towards positive values will produce a smaller overlapping region of incident type III beams, which do not excite SPPs (Figure S30j–l in the Supplementary Materials).

This overlapping produces the changes we see in the direct and Fourier space images relative to the zero-misalignment case shown in Figure S30d–f. The additional lobes seen in Figure 6i–l are also caused by the excitation of SPPs due to the roughness of the surface. Indeed, in addition to the momentum needed to excite SPPs with the grating, the extra momentum needed to excite SPPs can also be obtained by the scattering of the light due to roughness of the surface, which produce light with wavevectors in all directions [1,44].

4. Conclusions

The use of a spatial light modulator to generate vector LG beams allows us to dynamically excite surface plasmon polaritons in a circular Bragg grating. The unique properties of vector LG beams, particularly their polarization state, were exploited to selectively excite SPPs. Optical images both in the direct and Fourier spaces were taken with leakage radiation microscopy and analyzed, revealing that the excited SPPs gathered in the center of the grating. Our future research directions include exploring the potential of LG beams for exciting SPPs in complex geometries.

Supplementary Materials: The following supporting information can be downloaded at: https://www.mdpi.com/article/10.3390/opt5040039/s1.

Author Contributions: Conceptualization, V.R.-C. and R.S.-M.; methodology, V.R.-C. and R.S.-M.; software, A.P.-R. and R.S.-M.; validation, A.P.-R. and T.Z.; formal analysis, A.P.-R. and R.S.-M.; investigation, A.P.-R. and T.Z.; resources, V.R.-C. and R.S.-M.; data curation, A.P.-R. and R.S.-M.; writing—original draft preparation, R.S.-M.; writing—review and editing, V.R.-C.; visualization, A.P.-R. and R.S.-M.; supervision, R.S.-M.; project administration, R.S.-M.; funding acquisition, V.R.-C. and R.S.-M. All authors have read and agreed to the published version of the manuscript.

Funding: This research was funded by CONAHCYT-Mexico, grant number CB-133582, and by the China Scholarship Council, file number 202 008 070 054. This research was partially supported by the Graduate School NANO-PHOT (École Universitaire de Recherche, PIA3), grant number ANR-18-EURE-0013; by the French Ministry of Higher Education, Research, and Innovation (Ministère de l'Enseignement supérieur, de la Recherche et de l'Innovation, MESRI); and by the ECOS Nord program, grant number M19P01.

Data Availability Statement: The original contributions presented in this study are included in the Supplementary Materials; further inquiries can be directed to the corresponding authors.

Acknowledgments: This work was partially supported by the French HPC Center ROMEO, where the calculations shown in this work were performed. A. Peña-Ramírez thanks CONAHCyT for providing a scholarship for studying his PhD degree.

Conflicts of Interest: The authors declare no conflicts of interest.

Abbreviations

The following abbreviations are used in this manuscript:

SPPs	Surface plasmon polaritons
LG	Laguerre–Gauss
VB	Vector beam
SLM	Spatial light modulator
LRM	Leakage radiation microscopy
TM	Transverse magnetic
EBL	Electron beam lithography
PMMA	PolyMethyl MethAcrylate
CCD	Charge-coupled device
FDTD	Finite-difference time domain

References

1. Raether, H. *Surface Plasmons on Smooth and Rough Surfaces and on Gratings*; Springer Tracts in Modern Physics; Springer: Berlin/Heidelberg, Germany, 1988; Volume 111.
2. Zia, R.; Schuller, J.A.; Chandran, A.; Brongersma, M.L. Plasmonics: The next chip-scale technology. *Mater. Today* **2006**, *9*, 20 – 27. [CrossRef]
3. Ozbay, E. Plasmonics: Merging Photonics and Electronics at Nanoscale Dimensions. *Science* **2006**, *311*, 189. [CrossRef] [PubMed]
4. Barnes, W.L.; Dereux, A.; Ebbesen, T.W. Surface plasmon subwavelength optics. *Nature* **2003**, *424*, 824–830. [CrossRef] [PubMed]
5. Zayats, A.V.; Smolyaninov, I.I.; Maradudin, A.A. Nano-optics of surface plasmon polaritons. *Phys. Rep.* **2005**, *408*, 131 – 314. [CrossRef]
6. Kretschmann, E.; Raether, H. Notizen: Radiative Decay of Non Radiative Surface Plasmons Excited by Light. *Z. Naturforschung A* **1968**, *23*, 2135–2136. [CrossRef]
7. Otto, A. Excitation of nonradiative surface plasma waves in silver by the method of frustrated total reflection. *Z. Phys.* **1968**, *216*, 398–410. [CrossRef]
8. Lévêque, G.; Martin, O.J.F. Optimization of finite diffraction gratings for the excitation of surface plasmons. *J. Appl. Phys.* **2006**, *100*, 124301. [CrossRef]
9. de la Cruz, S.; Méndez, E.R.; Macías, D.; Salas-Montiel, R.; Adam, P.M. Compact surface structures for the efficient excitation of surface plasmon-polaritons. *Phys. Status Solidi B* **2012**, *249*, 1178–1187. [CrossRef]
10. Salomon, L.; Bassou, G.; Aourag, H.; Dufour, J.P.; de Fornel, F.; Carcenac, F.; Zayats, A.V. Local excitation of surface plasmon polaritons at discontinuities of a metal film: Theoretical analysis and optical near-field measurements. *Phys. Rev. B* **2002**, *65*, 125409. [CrossRef]
11. Yin, L.; Vlasko-Vlasov, V.K.; Pearson, J.; Hiller, J.M.; Hua, J.; Welp, U.; Brown, D.E.; Kimball, C.W. Subwavelength Focusing and Guiding of Surface Plasmons. *Nano Lett.* **2005**, *5*, 1399–1402. [CrossRef]
12. Tellez-Limon, R.; Fevrier, M.; Apuzzo, A.; Salas-Montiel, R.; Blaize, S. Theoretical analysis of Bloch mode propagation in an integrated chain of gold nanowires. *Photon. Res.* **2014**, *2*, 24–30. [CrossRef]
13. Tellez-Limon, R.; Fevrier, M.; Apuzzo, A.; Salas-Montiel, R.; Blaize, S. Numerical analysis of tip-localized surface plasmon resonances in periodic arrays of gold nanowires with triangular cross section. *J. Opt. Soc. Am. B* **2017**, *34*, 2147–2154. [CrossRef]
14. Tellez-Limon, R.; Blaize, S.; Gardillou, F.; Coello, V.; Salas-Montiel, R. Excitation of surface plasmon polaritons in a gold nanoslab on ion-exchanged waveguide technology. *Appl. Opt.* **2020**, *59*, 572–578. [CrossRef] [PubMed]
15. Hecht, B.; Bielefeldt, H.; Novotny, L.; Inouye, Y.; Pohl, D.W. Local Excitation, Scattering, and Interference of Surface Plasmons. *Phys. Rev. Lett.* **1996**, *77*, 1889–1892. [CrossRef] [PubMed]
16. Janunts, N.A.; Baghdasaryan, K.S.; Nerkararyan, K.V.; Hecht, B. Excitation and superfocusing of surface plasmon polaritons on a silver-coated optical fiber tip. *Opt. Commun.* **2005**, *253*, 118–124. [CrossRef]
17. Rui, G.; Zhan, Q. Tailoring optical complex fields with nano-metallic surfaces. *Nanophotonics* **2015**, *4*, 2–25. [CrossRef]
18. Shen, Y.; Wang, X.; Xie, Z.; Min, C.; Fu, X.; Liu, Q.; Gong, M.; Yuan, X. Optical vortices 30 years on: OAM manipulation from topological charge to multiple singularities. *Light. Sci. Appl.* **2019**, *8*, 90. [CrossRef]
19. Yao, A.M.; Padgett, M.J. Orbital angular momentum: Origins, behavior and applications. *Adv. Opt. Photonics* **2011**, *3*, 161–204. [CrossRef]
20. Yuan, G.H.; Wang, Q.; Tan, P.S.; Lin, J.; Yuan, X.C. A dynamic plasmonic manipulation technique assisted by phase modulation of an incident optical vortex beam. *Nanotechnology* **2012**, *23*, 385204. [CrossRef]

21. Wang, J. Data information transfer using complex optical fields: A review and perspective (Invited Paper). *Chin. Opt. Lett.* **2017**, *15*, 030005. [CrossRef]
22. Maurer, C.; Jesacher, A.; Fürhapter, S.; Bernet, S.; Ritsch-Marte, M. Tailoring of arbitrary optical vector beams. *New J. Phys.* **2007**, *9*, 78. [CrossRef]
23. Sancho-Parramon, J.; Bosch, S. Dark Modes and Fano Resonances in Plasmonic Clusters Excited by Cylindrical Vector Beams. *ACS Nano* **2012**, *6*, 8415–8423. [CrossRef] [PubMed]
24. Zang, X.; Bautista, G.; Turquet, L.; Setälä, T.; Kauranen, M.; Turunen, J. Efficient hybrid-mode excitation in plasmonic nanoantennas by tightly focused higher-order vector beams. *J. Opt. Soc. Am. B* **2021**, *38*, 521–529. [CrossRef]
25. Chen, W.; Abeysinghe, D.C.; Nelson, R.L.; Zhan, Q. Plasmonic Lens Made of Multiple Concentric Metallic Rings under Radially Polarized Illumination. *Nano Lett.* **2009**, *9*, 4320–4325. [CrossRef] [PubMed]
26. Gómez, D.E.; Teo, Z.Q.; Altissimo, M.; Davis, T.J.; Earl, S.; Roberts, A. The Dark Side of Plasmonics. *Nano Lett.* **2013**, *13*, 3722–3728. [CrossRef]
27. Tidwell, S.C.; Ford, D.H.; Kimura, W.D. Generating radially polarized beams interferometrically. *Appl. Opt.* **1990**, *29*, 2234–2239. [CrossRef]
28. Serrano-Trujillo, A.; Palafox, L.E.; Ruiz-Cortés, V. Study of spatially inhomogeneous polarized beams in a differential interference imaging technique. *Opt. Eng.* **2020**, *59*, 014105. [CrossRef]
29. Gorodetski, Y.; Shitrit, N.; Bretner, I.; Kleiner, V.; Hasman, E. Observation of Optical Spin Symmetry Breaking in Nanoapertures. *Nano Lett.* **2009**, *9*, 3016–3019. [CrossRef]
30. Gjonaj, B.; Aulbach, J.; Johnson, P.M.; Mosk, A.P.; Kuipers, L.; Lagendijk, A. Active spatial control of plasmonic fields. *Nat. Photonics* **2011**, *5*, 360–363. [CrossRef]
31. Genevet, P.; Lin, J.; Kats, M.A.; Capasso, F. Holographic detection of the orbital angular momentum of light with plasmonic photodiodes. *Nat. Commun.* **2012**, *3*, 1278. [CrossRef]
32. Liu, A.P.; Xiong, X.; Ren, X.F.; Cai, Y.J.; Rui, G.H.; Zhan, Q.W.; Guo, G.C.; Guo, G.P. Detecting orbital angular momentum through division-of-amplitude interference with a circular plasmonic lens. *Sci. Rep.* **2013**, *3*, 2402. [CrossRef] [PubMed]
33. Xiao, K.; Wei, S.; Min, C.; Yuan, G.; Zhu, S.W.; Lei, T.; Yuan, X.C. Dynamic cosine-Gauss plasmonic beam through phase control. *Opt. Express* **2014**, *22*, 13541–13546. [CrossRef] [PubMed]
34. Serrano-Trujillo, A.; Palafox, L.E.; Ruiz-Cortés, V. Engineering of cylindrical vector fields with a twisted nematic spatial light modulator. *Appl. Opt.* **2017**, *56*, 1310–1316. [CrossRef]
35. Drezet, A.; Hohenau, A.; Koller, D.; Stepanov, A.; Ditlbacher, H.; Steinberger, B.; Aussenegg, F.R.; Leitner, A.; Krenn, J.R. Leakage radiation microscopy of surface plasmon polaritons. *Mater. Sci. Eng. B* **2008**, *149*, 220–229. [CrossRef]
36. Mollet, O.; Cuche, A.; Drezet, A.; Huant, S. Leakage radiation microscopy of surface plasmons launched by a nanodiamond-based tip. *Diam. Relat. Mater.* **2011**, *20*, 995–998. [CrossRef]
37. Garcia-Ortiz, C.E.; Coello, V.; Han, Z.; Bozhevolnyi, S.I. Generation of diffraction-free plasmonic beams with one-dimensional Bessel profiles. *Opt. Lett.* **2013**, *38*, 905–907. [CrossRef]
38. Garcia-Ortiz, C.E.; Cortes, R.; Gómez-Correa, J.E.; Pisano, E.; Fiutowski, J.; Garcia-Ortiz, D.A.; Ruiz-Cortes, V.; Rubahn, H.G.; Coello, V. Plasmonic metasurface Luneburg lens. *Photonics Res.* **2019**, *7*, 1112–1118. [CrossRef]
39. Tovar, A.A. Production and propagation of cylindrically polarized Laguerre–Gaussian laser beams. *J. Opt. Soc. Am. A* **1998**, *15*, 2705–2711. [CrossRef]
40. Vyas, S.; Kozawa, Y.; Sato, S. Polarization singularities in superposition of vector beams. *Opt. Express* **2013**, *21*, 8972–8986. [CrossRef]
41. Vyas, S.; Kozawa, Y.; Miyamoto, Y. Creation of polarization gradients from superposition of counter propagating vector LG beams. *Opt. Express* **2015**, *23*, 33970–33979. [CrossRef]
42. Pinnell, J.; Nape, I.; Sephton, B.; Cox, M.A.; Rodríguez-Fajardo, V.; Forbes, A. Modal analysis of structured light with spatial light modulators: A practical tutorial. *J. Opt. Soc. Am. A* **2020**, *37*, C146–C160. [CrossRef] [PubMed]
43. Johnson, P.B.; Christy, R.W. Optical Constants of the Noble Metals. *Phys. Rev. B* **1972**, *6*, 4370–4379. [CrossRef]
44. Simon, H.J.; Guha, J.K. Directional surface plasmon scattering from silver films. *Opt. Commun.* **1976**, *18*, 391–394. [CrossRef]